Multi-Instrument Characterisation of Magnetospheric Cold Plasma Dynamics in the 22 June 2015 Geomagnetic Storm

Massimo Vellante[1], Kazue Takahashi[2], Alfredo Del Corpo[1], Irina S. Zhelavskaya[3], Jerry Goldstein[4], Ian Mann[5], Ermanno Pietropaolo[1], Jan Reda[6], and Balazs Heilig[7]

[1]University of L'Aquila
[2]The Johns Hopkins University Applied Physics Laboratory
[3]Helmholtz Centre Potsdam, GFZ German Research Centre For Geosciences, Potsdam, Germany
[4]SwRI
[5]University of Alberta
[6]Institute of Geophysics Polish Academy of Sciences
[7]Mining and Geological Survey of Hungary

November 22, 2022

Abstract

We present a comparison of magnetospheric plasma mass/electron density observations during an 11-day interval which includes the geomagnetic storm of 22 June 2015. For this study we used: equatorial plasma mass density derived from geomagnetic field line resonances (FLRs) detected by Van Allen Probes and at the ground-based magnetometer networks EMMA and CARISMA; in situ electron density inferred by the Neural-network-based Upper hybrid Resonance Determination algorithm applied to plasma wave Van Allen Probes measurements. The combined observations at L ~ 4, MLT ~ 16 of the two longitudinally-separated magnetometer networks show a temporal pattern very similar to that of the in situ observations: a density decrease by an order of magnitude about 1 day after the Dst minimum, a partial recovery a few hours later, and a new strong decrease soon after. The observations are consistent with the position of the measurement points with respect to the plasmasphere boundary as derived by a plasmapause test particle simulation. A comparison between plasma mass densities derived from ground and in situ FLR observations during favourable conjunctions shows a good agreement. We find however, for L < ~3, the spacecraft measurements to be higher than the corresponding ground observations with increasing deviation with decreasing L, which might be related to the rapid outbound spacecraft motion in that region. A statistical analysis of the average ion mass using simultaneous spacecraft measurements of mass and electron density indicates values close to 1 amu in plasmasphere and higher values (~ 2-3 amu) in plasmatrough.

Multi-Instrument Characterisation of Magnetospheric Cold Plasma Dynamics in the 22 June 2015 Geomagnetic Storm

M. Vellante[1], K. Takahashi[2], A. Del Corpo[1], I. S. Zhelavskaya[3], J. Goldstein[4], I. R. Mann[5], E. Pietropaolo[1], J. Reda[6], and B. Heilig[7]

[1]Department of Physical and Chemical Sciences, University of L'Aquila, L'Aquila, Italy.

[2]The Johns Hopkins University Applied Physics Laboratory, Laurel, MD, USA.

[3]Helmholtz Centre Potsdam, GFZ German Research Centre For Geosciences and University of Potsdam, Potsdam, Germany.

[4]Space Science and Engineering Division, Southwest Research Institute, San Antonio, Texas, USA.

[5]University of Alberta, Edmonton, AB, Canada.

[6]Institute of Geophysics, Polish Academy of Sciences, Warsaw, Poland

[7]Mining and Geological Survey of Hungary, Budapest, Hungary.

Corresponding author: Massimo Vellante (massimo.vellante@aquila.infn.it)

Key Points:

- The combination of two longitudinally-separated magnetometer arrays reproduces the main magnetospheric plasma density variations observed in situ
- Observations are consistent with predictions provided by a plasmapause test particle simulation
- Plasma mass densities derived from ground and in situ FLR observations for $L > 3$ are in good agreement during favourable conjunction intervals

Abstract

We present a comparison of magnetospheric plasma mass/electron density observations during an 11-day interval which includes the geomagnetic storm of 22 June 2015. For this study we used: equatorial plasma mass density derived from geomagnetic field line resonances (FLRs) detected by Van Allen Probes and at the ground-based magnetometer networks EMMA and CARISMA; in situ electron density inferred by the Neural-network-based Upper hybrid Resonance Determination algorithm applied to plasma wave Van Allen Probes measurements. The combined observations at L ~ 4, MLT ~ 16 of the two longitudinally-separated magnetometer networks show a temporal pattern very similar to that of the in situ observations: a density decrease by an order of magnitude about 1 day after the Dst minimum, a partial recovery a few hours later, and a new strong decrease soon after. The observations are consistent with the position of the measurement points with respect to the plasmasphere boundary as derived by a plasmapause test particle simulation. A comparison between plasma mass densities derived from ground and in situ FLR observations during favourable conjunctions shows a good agreement. We find however, for L < ~3, the spacecraft measurements to be higher than the corresponding ground observations with increasing deviation with decreasing L, which might be related to the rapid outbound spacecraft motion in that region. A statistical analysis of the average ion mass using simultaneous spacecraft measurements of mass and electron density indicates values close to 1 amu in plasmasphere and higher values (~ 2-3 amu) in plasmatrough.

1 Introduction

Understanding the concentration and composition of the plasma populating the Earth's magnetosphere, its spatial distribution and its temporal variations, represent a relevant information in the space weather context. In addition, the ability to reliably and routinely specify in-situ mass density dynamics using ground-based remote-sensing, especially during storms, would be a major step forward.

Electron and mass density of the magnetospheric plasma can be measured by different techniques both in space and from the ground. The electron number density can be measured locally by plasma wave experiments on board of satellites (Kurth et al., 2015) and remotely by ground detection of VLF whistlers propagating along the geomagnetic field lines (Park, 1972). On the other hand, the plasma mass density can be inferred from satellite (Takahashi et al., 2006) and ground (Menk & Waters, 2013) detection of geomagnetic field line resonances (FLR). In situ measurements of the concentration of different ions have been also reported (Horwitz et al., 1984; Sandhu et al., 2016), but spacecraft charging effects often prevent the detection of the ions in the low energy range (Moldwin, 1997).

Each of these measurements can provide information at a given time only at particular points in space and therefore, taken alone, provide only a very limited description of the dynamic processes occurring in the magnetosphere, especially along the world-line of individual satellites. Of course, in the absence of available in-situ satellite plasma measurements the ability to remote sense mass dynamics from the ground becomes of increased importance.

Global images of the plasmasphere (in terms of helium contribution) have been provided in the past from the EUV imager on the IMAGE satellite (Sandel et al., 2000). These images could be also converted to He^+ density maps in the equatorial plane (Sandel et al., 2003) allowing a quantitative comparison with other typical density measurements, but for conversion into total mass density it requires assumptions of the relative abundance of He^+, H^+ and other species. These global images revealed a lot of detailed structures in the plasmasphere (plumes, notches, channels, shoulders, etc.) which could be followed in their initial formation and time evolution in response to the variable conditions of the solar wind (Spasojević et al., 2003). No similar experiments are presently in operation (the IMAGE mission was operative from 2000 to 2005). It is therefore very important when investigating the dynamics of the magnetospheric plasma (for example during a geomagnetic storm) to combine as many measurements as possible at different locations and from different instruments/techniques to get a more complete picture of the ongoing processes. This is also important for the intercalibration of the different techniques.

It is also extremely useful for the interpretation of local variations to compare the observations with predictions provided by models and simulations. In this regard, the plasmapause test particle (PTP) simulation, which provides at any given time the global shape of the plasmapause using an ensamble of cold test particles subject to ExB drift, has been proven to be very effective (Goldstein et al., 2005, 2014a, 2014b).

Some coordinated ground-based and satellite observations have been conducted in the past (Carpenter et al., 1981; Clilverd et al., 2003; Dent et al., 2003, 2006; Grew et al., 2007; Maeda et al., 2009). These studies showed a good consistency among the different measurements and enabled in some cases to infer the concentration and the dynamics of the heavy ions during different geomagnetic activity conditions. Combined measurements of electron and mass density have been also conducted by using only in situ measurements from the same satellite (Nosé et al., 2011, 2015; Takahashi et al., 2006, 2008). These studies confirmed for example the formation of an oxygen torus near the plasmapause during the initial and recovery phase of a geomagnetic storm (Fraser et al., 2005).

In this paper we present a comparative study of plasma mass/electron density observations during an 11-day interval which includes the geomagnetic storm of 22 June 2015 (Dst minimum of −204 nT). The data used for this study are: a) equatorial plasma mass density derived from geomagnetic field line resonances (FLRs) detected at the ground-based magnetometer networks EMMA (Lichtenberger et al., 2013) and CARISMA (Mann et al., 2008); b) equatorial/local plasma mass density derived from FLRs detected by Van Allen Probes (Takahashi et al., 2015); c) in situ electron number density measurements by Van Allen Probes (Neural-network-based Upper hybrid Resonance Determination (NURD) data, Zhelavskaya et al., 2016). Measurements are also compared with the expected temporal evolution of the plasmapause shape from plasmapause test particle simulations (Goldstein et al., 2014b) available at http://enarc.space.swri.edu/PTP.

The remainder of the paper is organized as follows. Section 2 presents an overview of the examined interval and describes the experiments, data and methods used for the analysis. Section 3 presents a comparative study among the different kind of observations. Section 4 presents conclusions.

2 Data and Method

2.1 Ground Measurements

The event under study (18-28 June, 2015) was already examined in a previous paper (Piersanti et al., 2017) but using only plasma mass density estimates derived from EMMA-FLR observations. The adopted technique is comprehensively described in Del Corpo et al. (2019, 2020). Briefly, fundamental FLR frequencies were determined for the mid-point of 37 station pairs with a time step of half an hour, and then converted to equatorial plasma mass densities ρ_{eq} using the T02 Tsyganenko magnetic field model (Tsyganenko, 2002) and a radial dependence of the density along the field lines as given by the power law model:

$$\rho = \rho_{\mathrm{eq}}(r_{\mathrm{eq}}/r)^m, \tag{1}$$

where r is the geocentric distance, and r_{eq} is the equatorial distance. Following indications from previous studies (Vellante & Förster, 2006), we used a power law index m = 1. Equatorial densities were then evaluated at any given distance in the local time sector monitored by EMMA by applying a smoothing spline to the radial profiles (Del Corpo et al., 2019). As well known, at nighttime the low ionospheric conductivity generally prevents the formation of FLRs and therefore the method was usable only during daytime hours.

An overview of the temporal variation of the mass density for the event on a daily scale is shown in Figure 1 along with the geomagnetic indices Kp and Dst. The observations refer to the equatorial distances: 2.5, 3.0, 3.5, 4.0, 4.5, 5.0, 5.5 Earth radii (R_E) and two different magnetic local times (MLT): 10 and 16. Dashed horizontal lines in each panel indicate the density level of 22 June when the storm effects are not yet evident. In the morning sector (left panels) the density variation is characterized by a strong decrease on 24 June (1 day after the Dst minimum) for $r >=$ 3 R_E, followed by an almost complete recovery on the next day, a new decrease (even stronger) on 26 June, and a more gradual recovery on the next days. A similar pattern is observed on the afternoon sector but the recovery on 25 June was only partial.

Using a single meridional array we can monitor a given MLT region only every 24 hours. In order to increase the monitoring rate, we extended the analysis by using magnetometer data from the Alberta line (~ 310° CGM longitude) of the CARISMA network (Mann et al., 2008; https://www.carisma.ca) which is longitudinally separated from EMMA by ~150° (~10 hours in MLT). Station pairs which were available and useful for the present analysis are reported in Table 1. Figure 2 shows the mapping to the magnetic equatorial plane (using IGRF) of the EMMA (blue dots) and CARISMA (red dots) mid points of the station pairs used for the analysis. Longitude values, reported around the outermost circle in Figure 2, are expressed in terms of the difference between MLT and UT. CARISMA data were then processed for the whole period by applying the same technique used for the EMMA data. For the present study we restricted the analysis to r_{eq} = 4 R_E where the CARISMA data coverage was the best. As a matter of fact, this distance was generally very close to the equatorial region mapped by the MSTK-VULC pair (L = 3.83). It also corresponds to the mean equatorial radius of the plasmapause (Carpenter, 1968), and so it is a suitable location for monitoring the plasmasphere dynamics.

2.2 In Situ Measurements

During the investigated period the orbits of the Van Allen Probes, formerly known as Radiation Belt Storm Probes (RBSP), were characterized by outbound and inbound legs occurring in the daytime and night-time sectors, respectively. An example, for 24 June 2015, is shown in Figure 3 using L-MLT coordinates. The blue/red line refers to RBSP A/RBSP B, respectively, with Probe A preceding Probe B by ~ 1 hour. In the morning sector the Van Allen Probes were very close to the Earth (L < 2), so only the orbit section occurring in the afternoon was usable for a comparison with the daytime ground observations. In particular, the spacecraft crossed the L-shell = 4 at MLT ~ 16. The orbit characteristics changed little with time during the investigated period, so each Van Allen Probe crossed the same L-MLT region approximately every 9 hours.

We used RBSP electron number density values as derived by applying the NURD algorithm to plasma wave measurements (Zhelavskaya et al., 2016) which are freely available at the ftp://rbm.epss.ucla.edu/ftpdisk1/NURD/ ftp site. The data have a temporal resolution of 6 s and a variable uncertainty ranging from 10% to 14%.

We also used magnetic field (Kletzing et al., 2013) and electric field (Wygant et al., 2013) measurements made by both RBSP A and RBSP B to detect harmonic frequencies of toroidal mode standing Alfvén waves which were then converted to equatorial or local plasma mass density estimates. When expressed in magnetic field-aligned (MFA) coordinates, toroidal mode waves are identified in the azimuthal component of the magnetic field (B_ϕ) and in the radial component of the electric field (E_ν). Toroidal frequencies were then determined by first searching for peaks in the B_ϕ and E_ν power spectra which were computed in a moving 15 min data window shifted in 5-min steps. For each significant peak, a weighted average frequency (with the weight given by the corresponding power spectral density) was then computed within a given band around the spectral peak (see Takahashi et al., 2015 for more details). The top panel of Figure 4 shows the harmonic toroidal frequencies (fundamental, second, third, and fifth harmonic detected in B_ϕ, and the fundamental harmonic detected in E_ν) for the outbound leg of the orbit n. 2726 of RBSP B on 21 June 2015. The bottom panel of Figure 4 shows the corresponding estimates of the equatorial mass density derived from each detected harmonic frequency using the T02 magnetic field model and a radial dependence of the density along the field line $\propto r^{-1}$. The error associated to each estimate may have different sources (spectral method, poloidal-toroidal mode coupling, field line mapping, functional dependence of the density along the field line, etc.), but we expect the error to be larger for the densities derived from the fundamental harmonic because of the larger relative error in the frequency estimation. In any case, the example shows that the densities derived from different harmonics are consistent with each other. The red line is a smoothing spline applied to the experimental points and it is used to evaluate the density at any desired distance.

2.3 Plasmapause Test Particle Simulation

In order to provide contextual information for the local measurements, we used a plasmapause test particle (PTP) simulation (Goldstein et al., 2014b). Starting from an initial configuration specified by the Kp-based empirical plasmapause model of O'Brien and Moldwin (2003), the model predicts at any next time the global shape of the plasmapause in the equatorial plane using an ensamble of cold test particles subject only to ExB drift. The convection electric field is driven by solar wind data and the Kp geomagnetic index (see Godstein et al., 2014b, for further details). The PTP model has demonstrated its validity when compared to global images of the plasmasphere from IMAGE EUV (Goldstein et al., 2005), observations at geostationary orbit (Goldstein et al., 2014a), and Van Allen Probes observations (Goldstein et al., 2014b). In particular, Goldstein et al. (2014b) found that the mean difference in plasmapause encounter time between model and Van Allen Probes observations was about 30-40 min, and the mean model-observations difference in radial location was ~0.4 R_E. The output of the model (freely available at http://enarc.space.swri.edu/PTP/) provides the plasmapause location (in *L*-MLT coordinates) at a 15-min cadence, also in a movie format. For a direct comparison with the real observations, we generated virtual observations from this model at a given fixed point P_0 by constructing an index, I_{P0-PP}, in the following way (where d_{min} is the distance from P_0 to the plasmapause):

$I_{P0-PP} = 0$: P_0 outside the plasmasphere, $d_{min} > 0.4\ R_E$;

$I_{P0-PP} = 1$: P_0 outside the plasmasphere, $d_{min} \leq 0.4\ R_E$;

$I_{P0-PP} = 2$: P_0 inside the plasmasphere, $d_{min} \leq 0.4\ R_E$;

$I_{P0-PP} = 3$: P_0 inside the plasmasphere, $d_{min} > 0.4\ R_E$.

In the present study (see section 3.1), we considered the point of coordinates $L = 4$, MLT = 16.

2.4 Midnight Plasmapause Location as Derived From Swarm Measurements

Recenty, Heilig and Lühr (2013) found observational evidence for a close relationship between the position of the night side plasmapause and the inner boundary of small-scale (< 40 km) field-aligned currents (SSFACs) observed at low-Earth orbit, i.e. the *L*-shell across which the intensity of SSFACs increases by orders of magnitude. The correlation between the simultaneous variations of the two boundaries was found to be strongest near midnight, while at other MLTs the dayside plasmapause position correlates well with earlier observed position of the near-midnight SSFAC boundary. The observed time lag corresponds to the corotation time from sunrise to the MLT of the dayside plasmapause crossings. While the location of the SSFAC boundary was found very sensitive to the variations in geomagnetic activity, at a given disturbance level the boundary can be well fitted by a circle. Both the centre position and the radius of the circle depend on geomagnetic activity. Based on observations of ESA's Swarm satellites, Heilig and Lühr (2018) introduced a simple boundary model. Applying the model to observations made at any MLT, the midnight position of the boundary can be calculated as described in detail by Heilig and Lühr (2018). For this study, we derived a proxy of the midnight plasmapause position based on this approach. From the Swarm-detected SSFAC boundary positions, we first estimated the midnight boundary position. Then based on the validation results reported by Heilig and Lühr (2018), we subtracted 0.25 R_E from all values to account for the average distance between the two boundaries near midnight.

3 Comparative Study

3.1 Temporal Variation at *L* = 4, MLT = 16

We performed a comparison of the temporal variation observed by all of the measurement approaches described above at a fixed location in the magnetosphere during 18-28 June 2015 (Figure 5). Similar studies have been often used in the past using whistler measurements (Park, 1970, 1974), ground FLR measurements (Chi et al., 2000; Dent et al., 2006; Obana et al., 2010), and in situ measurements (Denton et al., 2012, 2016; Reinisch et al., 2004), especially for evaluating long-term density refilling rates after a depletion event. For the present study, because of the limitations imposed by the Van Allen Probes orbits and FLR measurements, the best point to monitor resulted to be L = 4, MLT = 16. The different kind of measurements were obtained as follows.

Equatorial mass density values inferred by EMMA/CARISMA observations (panel i) were obtained by interpolating the corresponding radial density profiles to fixed r_{eq} = 4 R_E at 14:00 UT/00:00 UT of each day.

Similarly, equatorial mass density values derived from FLRs detected by RBSP A and RBSP B (panels g-h) were obtained by interpolating the radial density profiles to fixed r_{eq} = 4 R_E (see description of Figure 4).

As regards the electron number density estimates from the NURD plasma wave technique (panels e-f), in order to reduce random measurement fluctuations, the original 6 sec data were logarithmically averaged over the interval corresponding to the outbound transit time between the L-shells 3.9 and 4.1 (~ 8.5 min). The magnetic latitude of the spacecraft at these passes was always less than 15°, so for the present analysis, no corrections were made to take into account of different distances from the equator from pass to pass. For example, assuming a density variation of r^{-1} along the field line, the density value at a latitude of 15° would be only 7% lower than at the equator.

Lines connecting data points are drawn to guide the eye. They are drawn as dashed lines (panels g-h) when data are missing between two consecutive observations. For each panel the mean MLT value and the corresponding standard deviation is also indicated.

Also shown in the four uppermost panels (a-d) are the Dst index, the Kp index, the hourly averages of the Z-component of the interplanetary magnetic field (IMF) in GSM coordinates (solar wind OMNI data), and the hourly averages of the midnight plasmapause proxy as derived from Swarm observations (see section 2.4). The black line in panel (d) is a smoothing spline through the data. Note the very good correspondence of the midnight plasmasphere erosion phases observed in panel (d) with the intervals of southward direction of $B_{z,IMF}$ (highlighted in red in panel (c)). The greatest erosion occurred at the beginning of 23 June (in correspondence with the Dst minimum) with the midnight plasmapause retreating down to ~2 R_E.

As can be seen, the temporal variation is remarkably similar for all density measurements. In particular, the same sequence of decrease and increase through 23-25 June is observed. This pattern could not have been observed at ground if only one latitudinal array (as in Figure 1) had been used. Note also the delay in the afternoon density depletions with respect to the midnight plasmasphere contractions, which is compatible with the time required by the night-time plasmasphere to corotate into the afternoon sector.

The almost full recovery observed in the middle of 24 and 25 June appears too quick to be attributed to a refilling from the ionosphere. Indeed, both theoretical arguments (e.g., Rasmussen et al., 1993) and previous experimental observations (Obana et al., 2010; Park, 1974) indicate a duration of several days for an L = 4 flux tube to refill after a storm-associated depletion. A more likely explanation is that an extended plasmasphere structure drifted through the observation point (Denton et al., 2012; Reinisch et al., 2004).

This hypothesis is supported by the virtual observations from the plasmapause test particle (PTP) simulation reported in the bottom panel of Figure 5 in terms of the $I_{P0\text{-}PP}$ index defined in section 2.3. Values above/below the horizontal dashed line mean that the monitored point is in plasmasphere (PS)/plasmatrough (PT). As can be seen, the virtual observations are qualitatively consistent with the real observations. In particular the index mimics the sequence of the up and down density variations observed during 24-25 June. Also worth of note is the correspondence in the strong density increase observed through the first half of 18 June.

An overview of the global evolution of the simulated plasmasphere during 24-25 June is shown in Figure 6, with one snapshot every 4 h. The times of these snapshots are marked in Figure 5j with dotted vertical lines. Also indicated in each snapshot are the RBSP A and B locations and orbits, the monitored point at L = 4, 16 MLT (orange dot), and the midnight plasmapause location as determined from Swarm observations (black cross). According to the simulation, the density increase observed in the middle of 24 June is interpretable in terms of the rotation of a drainage plume through the monitored point. The increase on the next day (25 June) would be due instead to the sunward surge of the plasma (snapshot at 08 UT) caused by a new enhancement of the convection, as testified by the increase of Kp at 06-09 UT (Figure 5b) and a corresponding southward turning of $B_{z,IMF}$ (Figure 5c). The subsequent plume rotation, when the convection subsided, brought the monitored point to be back outside the plasmasphere at the end of 25 June. Note also that for the 10 MLT sector, the strong decrease on 24 June followed by an almost complete recovery on 25 June observed by EMMA (left panels of Figure 1) is consistent with the corresponding snapshots at 08 UT in Figure 6. In fact, on 24 June 08 UT, at 10 MLT (blue straight line) the plasmapause is located at ~3.4 R_E, and 24 hours later at ~5.2 R_E. Also worth of note is the general good agreement of the Swarm-derived midnight plasmapause location (black cross) with that expected from the PTP simulation.

3.2 Conjunction Study

We also conducted a more detailed comparison between space and ground measurements by restricting the analysis to favourable conjunction periods. Fairly good conjunction occurred every eighth RBSP orbit, i.e. every third day (on 22, 25, and 28 June 2015). The list of the selected intervals is reported in Table 2, where the start-end time in the last column is the time interval covered by the RBSP-FLR measurements. Figure 7 shows the locations of the EMMA stations in geographic coordinates along with the magnetic field footprints of RBSP A and B for the six intervals reported in Table 2. The footprints in Figure 7 (red/blue dots) are evaluated in correspondence of each detected toroidal frequency measurement made every 5 min and are obtained using the T02 magnetic field model.

The results of the ground-space comparison for each of the selected intervals are shown in Figure 8. The red points are the RBSP equatorial mass densities derived from the toroidal frequencies evaluated at a 5-min time step. The inversion procedure was applied to all detected harmonics, so different density estimates may be present at a given time. For each RBSP measurement, the closest in time EMMA radial density profile was fitted by a smoothing spline and the fitting value at the RBSP position was taken. These EMMA values are indicated in Figure 8 with blue open circles. The electron density profile (NURD data) is also shown as a black solid line for the entire outbound leg. The original 6-s local measurements were first converted in equatorial values assuming a radial distribution along the field line $\propto r^{-1}$ and then a smoothing spline was applied to reduce short-scale fluctuations due to measurement errors. The dashed curve is the Carpenter and Anderson (1992) saturated plasmasphere electron density model which is drawn as a useful reference. The measurements are plotted as a function of UT, and reference L values (and corresponding MLT values) are indicated by dotted vertical lines. The mean MLT deviation (ΔMLT) between EMMA and RBSP measurements is also indicated.

There is a general good agreement between ground and space mass density estimates. Mass density values (in amu cm^{-3}) are also generally close to electron number density values (in cm^{-3}), which would be consistent with a plasma composed mainly of hydrogen ions. The largest discrepancy is observed in panel (d) where, for r > 5 R_E (outward of an abrupt density falloff), both RBSP and EMMA mass density values are significantly above the electron number density level, up to a factor of ~8. This might be indicative of the presence of an oxygen torus just outward of the plasmapause (Fraser et al., 2005).

There is also some indication for the RBSP and EMMA mass density profiles to diverge with decreasing distance in the range $2 < L < 3$ (see panels (c), (d), (e), (f)), the RBSP estimates being higher than the corresponding EMMA estimates.

The observations for these conjunction events have been statistically analyzed and the results are shown in Figure 9. Panel (a) shows the equatorial density ratio ρ_{RBSP}/ρ_{EMMA} as a function of r_{eq}. 105 sample pairs were available for this analysis. The different markers/colors indicate from which harmonic the RBSP estimate was obtained. The lower quartile (0.96), the median (1.14), and the upper quartile (1.34) of the whole population are indicated on the top. The black dots connected by straight lines are the medians in r_{eq} bins, and the vertical bars connect the lower and upper quartiles. The number of samples and medians for each bin are also indicated above the horizontal axis. These results indicate a very good agreement between plasma mass densities derived from ground and in situ FLR observations at all distances, but also confirm systematically higher RBSP estimates for $r_{eq} < 3$ R_E.

Panel (b) is the plot of the local RBSP mass density over the corresponding electron number density, i.e. the estimated local average ion mass M. The RBSP mass densities are the same used in panel (a) but converted to local mass densities at the RBSP position assuming a density variation of r^{-1} along the field. The electron number density values were obtained by taking a log average over 5-min windows around the central time of the FLR measurements. The results look very similar to those of panel (a). The higher M values obtained for $r_{eq} < 3$ R_E are then possibly due to an overestimation of the mass density (underestimation of the FLR frequency) from the spacecraft data rather than to a real increase of the average ion mass (see discussion below).

Panel (c) is the plot of the local average ion mass, but using EMMA measurements for the mass density. As expected from the results of panels (a) and (b), the M values are slightly lower and closer to 1 amu, even for $r_{eq} < 3$ R_E.

The previous results are restricted to the time intervals with good RBSP-EMMA conjunction. In Figure 10a the analysis of the average ion mass is extended using the whole RBSP-FLR data set for 18-28 June 2015. For a better consistency with the previous analysis only outbound passes were considered. 1182 data points were available, i.e. a much larger data set with respect to that used in Figure 9b. The median values are practically identical to those of Figure 9b, except for slightly higher values (~ 20%) for $r_{eq} > 4\ R_E$.

A clear increase of M for $r_{eq} < 3\ R_E$ is confirmed even for this larger data set. Since we do not find a similar effect when using ground observations (Figure 9c), we argue that it could be due to a downward frequency shift caused by the faster cross-L movement of the spacecraft at lower L values. More specifically, during the investigated interval, the RBSP cross-L velocity was maximum at $L \sim 1.8$. A similar effect was previously found by Anderson et al. (1989), Vellante et al. (2004), Heilig et al. (2013), and Takahashi et al. (2015). The frequency shift was theoretically interpreted either by considering each crossed L-shell oscillating at its own resonance frequency (Anderson et al., 1989), or by considering the satellite movement across the resonance region in case of a monochromatic driving wave (Vellante et al., 2004). In the present study, no RBSP-FLR measurements were available during inbound passes at $L < 3$, so we could not verify the expected opposite effect, i.e. a mass density underestimate due to an upward frequency shift. Another (or additional) possible cause of the higher M medians for $r_{eq} < 3\ R_E$ could be a downward bias in the frequency estimate due to the weighted averaging method which was adopted in the frequency selection (section 2.2). Indeed, due to the typical power law decrease with frequency of the background power spectral density, the frequencies on the left of the spectral peak have on average a larger weight with respect to the frequencies to the right of the peak. This effect should increase with decreasing frequency, and then might be more significant for $r_{eq} < 3\ R_E$ where the fundamental frequency samples are dominant. We evaluated that in some cases the corresponding density overestimation could be up to ~20%.

An M value of 1.2 amu, found in this analysis in the range $3\ R_E < r_{eq} < 6\ R_E$, is typical for the plasmasphere (Nosé et al., 2015; Takahashi et al., 2015) which is dominated by H^+ ions. Larger values (~ 3-7 amu) were found, instead, in the plasmatrough by Takahashi et al. (2006, 2008) and Nosé et al. (2011, 2015), using the same technique of the present paper. In order to separate plasmaspheric-like from trough-like observations, we used the same empirical criterion adopted by Sheeley et al. (2001), i.e. we considered an observation to refer to the plasmasphere/plasmatrough region if the local electron number density was higher/lower than the separation value given by the following expression $n_o = 10\ (6.6/L)^4$. Figure 10b shows in fact that the electron number density values (black dots) are distributed in two different groups which are quite well separated by the threshold density n_o (red line). Also shown in the figure is the Carpenter and Anderson (1992) saturated plasmasphere electron density model (blue line). After using this criterion, we found for the plasmatrough a moderate increase in the estimated average ion mass: a median value of 1.55 amu when considering the whole population (398 data pairs) and a maximum median value of 3.0 amu in the 3.0-3.5 R_E bin.

Lastly, we examined the effect of using a different power law dependence of the mass density along the field line. All results discussed so far have been obtained by using a power law index $m = 1$ in equation (1). We considered reasonable to assume as a possible range of the power law index: $0 <= m <= 2$. For example, Takahashi et al. (2006) and Nosé et al. (2015) used $m = 0.5$. We found no significant differences when using $m = 0$, or $m = 2$ instead of $m = 1$. For example, the median value for the whole population in panel (d) changed to 1.32 for $m = 0$ and 1.16 when using $m = 2$. The maximum change occurred in the highest r_{eq} bin (6-6.5 R_E) with a variation of $\sim \pm 10\%$.

4 Conclusions

The detection of geomagnetic field line resonances by ground-based magnetometer arrays is a very useful tool for remote sensing temporal and spatial variations of the magnetospheric plasma mass density. For example it has been applied successfully for a) identifying the plasmapause (Del Corpo et al., 2020; Kale et al., 2007; Menk et al., 2004; Milling et al., 2001), b) studying the diurnal (Chi et al., 2013; Del Corpo et al., 2019; Waters et al., 1994) and annual (Berube et al., 2003; Menk et al., 2012; Vellante et al., 2007) variations, c) examining the dependence on the solar EUV irradiance (Vellante et al., 2007), d) constructing an empirical model in the equatorial plane (Berube et al., 2005; Del Corpo et al., 2020).

The FLR-technique has been also used to investigate magnetospheric density variations during geomagnetic storms with particular regard to the study of plasmasphere erosion and subsequent refilling from the ionosphere (Chi et al., 2000, 2005; Dent et al., 2006; Grew et al., 2007; Kale et al., 2009; Lichtenberger et al., 2013; Obana et al., 2010; Pezzopane et al., 2019; Piersanti et al., 2017; Villante et al., 2006). However, the use of a single meridional array (which can monitor only one longitudinal sector) does not allow to get a global picture of the spatio-temporal plasma dynamics during these processes. In addition, without contextual information provided by global observations or models, the causes of the observed variations may not be unambiguously determined.

In the present paper, we found that by combining the observations from two meridional magnetometer arrays (EMMA and CARISMA) longitudinally separated by ~10 hours in local time, we can reproduce the main variations in plasma density observed by the RBSP spacecraft on consecutive passes (every ~9 hours) through the same magnetospheric region (L = 4, 16 MLT) during a disturbed period. In addition, the supporting information provided by a plasmapause test particle simulation was crucial to correctly interpret the causes of such variations. In particular, the PTP simulation allowed to interpret rapid recoveries observed after strong density depletions as due to the passage of a drainage plume through the measurement point in one case, and to the sunward surge of the plasma at the beginning of a magnetospheric convection enhancement in another case. So in general, the approach of combining ground remote sensing of mass density using arrays from different longitudes results to be effective for diagnosing the spatio-temporal mass dynamics associated with the advection of dense plasma which occurs locally on much shorter timescales than plasmaspheric refilling. Obviously more latitudinal chains would be able to reveal more detailed information.

We also conducted a direct comparison between the plasma mass densities derived from ground FLR observations and those derived from space FLR observations for favourable conjunction events. 105 measurements could be compared in the L-range 2-6. To our knowledge, this is the most extensive direct comparison between ground and space FLR measurements. Quite a good agreement was found between the plasma mass densities inferred from the two kind of measurements, with the in situ density estimates being on average 10% higher than the corresponding ground estimates. Larger deviations were found for L < ~3, up to a factor of ~2 at L ~2. This result is qualitatively consistent with a downward shift in the frequency observed by a spacecraft moving outward across the L shells, which is expected to increase with decreasing radial distance because of the increasing spacecraft cross-L velocity.

An analysis of the average ion mass using simultaneous RBSP measurements of the mass and electron number density indicates an average ion mass close to 1 amu in the plasmasphere and higher values (typically ~ 2-3 amu, and up to ~ 8 amu) in the plasmatrough, consistent with previous observations (Nosé et al., 2011, 2015; Takahashi et al., 2006, 2008).

Acknowledgments

Work at University of L'Aquila was supported by Italian MIUR-PRIN grant 2017APKP7T_004 on *Circumterrestrial Environment: Impact of Sun-Earth Interaction*. K.T. was supported by NASA Grants NNX17AD34G and 80NSSC20K1446. CARISMA is operated by the University of Alberta, funded by the Canadian Space Agency. IRM is supported by a Discovery Grant from Canadian NSERC. The development of the Swarm plasmapause proxy at GFZ German Research Centre for Geosciences, Potsdam (B.H.) is supported through an ESA Swarm DISC activity (CCN 2 to ESRIN Contract No. 4000109587/13/I-NB). We thank the Finnish Meteorological Institute (FMI), the University of Oulu (Finland), the Institute of Geophysics of the Polish Academy of Sciences (IGF-PAS), the Mining and Geological Survey of Hungary (MBFSZ) and the University of L'Aquila for contributing to EMMA. International Space Science Institute (ISSI, Bern) facilitated collaboration of M.V., K.T., A.D.C., and B.H. by hosting meetings of the team "Investigating the Magnetosphere through Magnetoseismology" (led by Peter Chi, USA). Data used in this study are available from the following sources: Zenodo (https://doi.org/10.5281/zenodo.4534059) for EMMA data; NASA/GSFC Space Physics Data Facility Coordinated Data Analysis Web (https://cdaweb.gsfc.nasa.gov) for magnetic and electric field measurements by Van Allen Probes and for OMNI; World Data Center for Geomagnetism, Kyoto (http://wdc.kugi.kyoto-u.ac.jp) for geomagnetic indices; GFZ Data Services: https://dataservices.gfz-potsdam.de/panmetaworks/showshort.php?id=escidoc:5098892 (Zhelavskaya et al., 2020) and Department of Earth, Planetary, and Space Sciences, University of California, Los Angeles, California (ftp://rbm.epss.ucla.edu/ftpdisk1/NURD) for NURD electron density data; University of Alberta, Edmonton, Canada (https://www.carisma.ca) for CARISMA data; Space Science and Engineering Division, Southwest Research Institute, San Antonio, Texas (http://enarc.space.swri.edu/PTP) for Plasmapause Test Particle (PTP) Simulations. The SSFAC boundary positions and the plasmapause position proxy used in this study will be available from 1 Apr, 2021 as the Midnight Plasmapause Index (PPI) L2 product through the Swarm dissemination portal (https://swarm-diss.eo.esa.int/).

References

Anderson, B. J., Engebretson, M. J., & Zanetti, L. J. (1989). Distortion effects in spacecraft observations of MHD toroidal standing waves: Theory and observations. *Journal of Geophysical Research*, *94*(A10), 13425–13445. https://doi.org/10.1029/JA094iA10p13425

Berube, D., Moldwin, M. B., Fung, S. F., & Green, J. L. (2005). A plasmaspheric mass density model and constraints on its heavy ion concentration. *Journal of Geophysical Research*, *110*, A04212. https://doi.org/10.1029/2004JA010684

Berube, D., Moldwin, M. B., & Weygand, J. M. (2003). An automated method for the detection of field line resonance frequencies using ground magnetometer techniques. *Journal of Geophysical Research*, *108*, 1348. https://doi.org/10.1029/2002JA009737, A9

Carpenter, D. L. (1968). Recent Research on the Magnetospheric Plasmapause, *Radio Science*, *3*. https://doi.org/10.1002/rds196837719

Carpenter, D. L., & Anderson, R. R. (1992). An ISEE/whistler model of equatorial electron density in the magnetosphere. *Journal of Geophysical Research*, *97*(A2), 1097–1108. https://doi.org/10.1029/91JA01548

Carpenter, D. L., Anderson, R. R., Bell, T. F., & Miller, T. R. (1981). A comparison of equatorial electron densities measured by whistlers and by a satellite radio technique. *Geophysical Research Letters*, *8*: 1107-1110. https://doi.org/10.1029/GL008i010p01107

Chi, P. J., Engebretson, M. J., Moldwin, M. B., Russell, C. T., Mann, I. R., Hairston, M. R., et al. (2013). Sounding of the plasmasphere by Mid-continent MAgnetoseismic Chain (McMAC) magnetometers. *Journal of Geophysical Research: Space Physics*, *118*, 3077–3086. https://doi.org/10.1002/jgra.50274

Chi, P. J., Russell, C. T., Foster, J. C., Moldwin, M. B., Engebretson, M. J., & Mann, I. R. (2005). Density enhancement in plasmasphere-ionosphere plasma during the 2003 Halloween Superstorm: Observations along the 330th magnetic meridian in North America. *Geophysical Research Letters*, *32*, L03S07. https://doi.org/10.1029/2004GL021722

Chi, P. J., Russell, C. T., Musman, S., Peterson, W. K., Le, G., Angelopoulos, V., et al. (2000). Plasmaspheric depletion and refilling associated with the September 25, 1998 magnetic storm observed by ground magnetometers at $L = 2$. *Geophysical Research Letters*, *27*(5), 633–636. https://doi.org/10.1029/1999GL010722

Clilverd, M. A., Menk, F. W., Milinevski, G., Sandel, B. R., Goldstein, J., Reinisch, B. W., et al. (2003). In situ and ground-based intercalibration measurements of plasma density at $L = 2.5$. *Journal of Geophysical Research*, *108,* 1365. https://doi.org/10.1029/2003JA009866, A10

Del Corpo, A., Vellante, M., Heilig, B., Pietropaolo, E., Reda, J., & Lichtenberger, J. (2019). Observing the cold plasma in the Earth's magnetosphere with the EMMA network. *Annals of Geophysics*, *62*(4), GM447. https://doi.org/10.4401/ag-7751

Del Corpo, A., Vellante, M., Heilig, B., Pietropaolo, E., Reda, J., & Lichtenberger, J. (2020). An empirical model for the dayside magnetospheric plasma mass density derived from EMMA magnetometer network observations. *Journal of Geophysical Research: Space Physics*, *125*, e2019JA027381. https://doi.org/10.1029/2019JA027381

Dent, Z. C., Mann, I. R., Goldstein, J., Menk, F. W., & Ozeke, L. G. (2006). Plasmaspheric depletion, refilling, and plasmapause dynamics: A coordinated ground-based and IMAGE satellite study. *Journal of Geophysical Research*, *111*, A03205. https://doi.org/10.1029/2005JA011046

Dent, Z. C., Mann, I. R., Menk, F. W., Goldstein, J., Wilford, C. R., Clilverd, M. A., & Ozeke, L. G. (2003). A coordinated ground-based and IMAGE satellite study of quiet-time plasmaspheric density profiles. *Geophysical Research Letters*, *30*, 1600. https://doi.org://10.1029/2003GL016946, 12

Denton, R. E., Takahashi, K., Amoh, J., & Singer, H. J. (2016). Mass density at geostationary orbit and apparent mass refilling. *Journal of Geophysical Research: Space Physics*, *121*, 2962–2975. https://doi.org/10.1002/2015JA022167

Denton, R. E.,Wang, Y.,Webb, P. A., Tengdin, P.M., Goldstein, J., Redfern, J. A., & Reinisch, B.W. (2012). Magnetospheric electron density long-term (> 1 day) refilling rates inferred from passive radio emissions measured by IMAGE RPI during geomagnetically quiet times. *Journal of Geophysical Research*, *117*, A03221. https://doi.org/10.1029/2011JA017274

Fraser, B. J., Horwitz, J. L., Slavin, J. A., Dent, Z. C., & Mann, I. R. (2005). Heavy ion mass loading of the geomagnetic field near the plasmapause and ULF wave implications. *Geophysical Research Letters*, *32*, L04102. https://doi.org/10.1029/2004GL021315

Goldstein, J., De Pascuale, S., Kletzing, C., Kurth, W., Genestreti, K. J., Skoug, R. M., et al. (2014b). Simulation of Van Allen Probes plasmapause encounters. *Journal of Geophysical Research: Space Physics*, *119*, 7464–7484. https://doi.org/10.1002/2014JA020252

Goldstein, J., Sandel, B. R., Forrester, W. T., Thomsen, M. F., & Hairston, M. R. (2005). Global plasmasphere evolution 22–23 April 2001. *Journal of Geophysical Research.*, *110*, A12218. https://doi.org/10.1029/2005JA011282

Goldstein, J., Thomsen, M. F., & DeJong, A. (2014a). In situ signatures of residual plasmaspheric plumes: Observations and simulation. *Journal of Geophysical Research: Space Physics*, *119*, 4706–4722. https://doi.org/10.1002/2014JA019953

Grew, R. S., Menk, F. W., Clilverd, M. A., & Sandel, B. R. (2007). Mass and electron densities in the inner magnetosphere during a prolonged disturbed interval. *Geophysical Research Letters*, *34*, L02108. https://doi.org/10.1029/2006GL028254

Heilig, B., & Lühr, H. (2013). New plasmapause model derived from CHAMP field-aligned current signatures, *Annales Geophysicae*, *31*, 529-539. https://doi.org/10.5194/angeo-31-529-2013

Heilig, B., & Lühr, H. (2018). Quantifying the relationship between the plasmapause and the inner boundary of small-scale field-aligned currents, as deduced from Swarm observations, *Annales Geophysicae*, *36*, 595-607. https://doi.org/10.5194/angeo-36-595-2018

Heilig, B., Sutcliffe, P. R., Ndiitwani, D. C., & Collier, A. B. (2013). Statistical study of geomagnetic field line resonances observed by CHAMP and on the ground. *Journal of Geophysical Research: Space Physics*, *118*, 1934–1947. https://doi.org/10.1002/jgra.50215

Horwitz, J. L., Comfort, R. H., & Chappell, C. R. (1984). Thermal ion composition measurements of the formation of the new outer plasmasphere and double plasmapause during storm recovery phase. *Geophysical Research Letters*, *11*, 701–704. https://doi.org/10.1029/GL011i008p00701

Kale, Z. C., Mann, I. R., Waters, C. L., Goldstein, J., Menk, F. W., & Ozeke, L. G. (2007). Ground magnetometer observation of a cross-phase reversal at a steep plasmapause. *Journal of Geophysical Research*, *112*, A10222. https://doi.org/10.1029/2007JA012367

Kale, Z. C., Mann, I. R., Waters, C. L., Vellante, M., Zhang, T. L., & Honary, F. (2009). Plasmaspheric dynamics resulting from the Hallowe'en 2003 geomagnetic storms. *Journal of Geophysical Research*, *114*, A08204. https://doi.org/10.1029/2009JA014194

Kletzing, C. A., Kurth, W. S., Acuna, M., MacDowall, R. J., Torbert, R. B., Averkamp, T., et al. (2013). The Electric and Magnetic Field Instrument Suite and Integrated Science (EMFISIS) on RBSP. *Space Science Reviews*, *179*, 127–181. https://doi.org/10.1007/s11214-013-9993-6

Kurth, W. S., De Pascuale, S., Faden, J. B., Kletzing, C. A., Hospodarsky, G. B., Thaller, S., & Wygant, J. R. (2015). Electron densities inferred from plasma wave spectra obtained by the Waves instrument on Van Allen Probes. *Journal of Geophysical Research: Space Physics*, *120*. https://doi.org/10.1002/2014JA020857

Lichtenberger, J., Clilverd, M. A., Heilig, B., Vellante, M., Manninen, J., Rodger, C. J., et al. (2013). The plasmasphere during a space weather event: First results from the PLASMON project. *Journal of Space Weather and Space Climate*, *3*, A23. https://doi.org/10.1051/swsc/2013045

Maeda, N., Takasaki, S., Kawano, H., Ohtani, S., Décréau, P. M. E., Trotignon, J. G., et al. (2009). Simultaneous observations of the plasma density on the same field line by the CPMN ground magnetometers and the Cluster satellites. *Advances in Space Research*, *43*(2), 265-272. https://doi.org/10.1016/j.asr.2008.04.016

Mann, I. R., Milling, D. K., Rae, I. J., Ozeke, L. G., Kale, A., Kale, Z. C., et al. (2008). The Upgraded CARISMA Magnetometer Array in the THEMIS Era. *Space Science Reviews*, *141*, 413–451. https://doi.org/10.1007/s11214-008-9457-6

Menk, F. W., Ables, S. T., Grew, R. S., Clilverd, M. A., & Sandel, B. R. (2012). The annual and longitudinal variations in plasmaspheric ion density. *Journal of Geophysical Research*, *117*, A03215, https://doi.org/10.1029/2011JA017071

Menk, F. W., Mann, I. R., Smith, A. J., Waters, C. L., Clilverd, M. A., & Milling, D. K. (2004). Monitoring the plasmapause using geomagnetic field line resonances. *Journal of Geophysical Research*, *109*, A04216. https://doi.org/10.1029/2003JA010097

Menk, F. W., & Waters, C. L. (2013). *Magnetoseismology: Ground-Based Remote Sensing of Earth's Magnetosphere*. Weinheim, Germany: John Wiley & Sons, Inc. https://doi.org/10.1002/9783527652051

Milling, D. K., Mann, I. R., & Menk, F. W. (2001). Diagnosing the plasmapause with a network of closely spaced ground-based magnetometers. *Geophysical Research Letters*, *28*(1), 115-118. https://doi.org/10.1029/2000GL011935

Moldwin, M.B. (1997). Outer Plasmaspheric Plasma Properties: What We Know from Satellite Data. *Space Science Reviews 80*, 181–198. https://doi.org/10.1023/A:1004921903897

Nosé, M., Oimatsu, S., Keika, K., Kletzing, C. A., Kurth, W. S., De Pascuale, S., et al. (2015). Formation of the oxygen torus in the inner magnetosphere: Van Allen Probes observations. *Journal of Geophysical Research: Space Physics*, *120*, 1182– 1196. https://doi.org/10.1002/2014JA020593.

Nosé, M., Takahashi, K., Anderson, R. R., & Singer, H. J. (2011). Oxygen torus in the deep inner magnetosphere and its contribution to recurrent process of O^+-rich ring current formation. *Journal of Geophysical Research*, *116*, A10224, https://doi.org/10.1029/2011JA016651

Obana, Y., Menk, F. W., & Yoshikawa, I. (2010). Plasma refilling rates for L = 2.3-3.8 flux tubes. *Journal of Geophysical Research*, *115*, A03204. https://doi.org/10.1029/2009JA014191

O'Brien, T. P., & Moldwin, M. B. (2003). Empirical plasmapause models from magnetic indices. *Geophysical Research Letters*, *30*, 1152. https://doi.org/10.1029/2002GL016007, 4

Park, C. G. (1970). Whistler observations of the interchange of ionization between the ionosphere and the protonosphere. *Journal of Geophysical Research*, *75*(22), 4249–4260. https://doi.org/10.1029/JA075i022p04249

Park, C. G. (1972). Methods of determining electron concentrations in the magnetosphere from nose whistlers. Technical Report 3454-1, Radioscience Laboratory, Stanford Electronics Laboratories, Stanford University, Stanford, California (USA).

Park, C. G. (1974). Some features of plasma distribution in the plasmasphere deduced from Antarctic whistlers. *Journal of Geophysical Research*, *79*(1), 169–173. https://doi.org/10.1029/JA079i001p00169

Pezzopane, M., Del Corpo, A., Piersanti, M., Cesaroni, C., Pignalberi, A., Di Matteo, S., et al. (2019). On some features characterizing the plasmasphere-magnetosphere-ionosphere system during the geomagnetic storm of 27 May 2017. *Earth, Planets and Space*, *71*, 77. https://doi.org/10.1186/s40623-019-1056-0

Piersanti, M., Alberti, T., Bemporad, A., Berrilli, F., Bruno, R., Capparelli, V., et al. (2017). Comprehensive analysis of the geoeffective solar event of 21 June 2015: Effects on the magnetosphere, plasmasphere, and ionosphere systems. *Solar Physics*, *292*(11), 169. https://doi.org/10.1007/s11207-017-1186-0

Rasmussen, C. E, Guiter, S. M., & Thomas, S. G. (1993). A two-dimensional model of the plasmasphere: refilling time constants. *Planetary and Space Science*, *41*(1):35–43. https://doi.org/10.1016/0032-0633(93)90015-T

Reinisch, B. W., Huang, X., Song, P., Green, J. L., Fung, S. F., Vasyliunas, V. M., et al. (2004). Plasmaspheric mass loss and refilling as a result of a magnetic storm. *Journal of Geophysical Research*, *109*, A01202. https://doi.org/10.1029/2003JA009948

Sandel, B. R., Broadfoot, A. L., Curtis, C. C., King, R. A., Stone, T. C., Hill, R. H., et al. (2000). The Extreme Ultraviolet Imager Investigation for the IMAGE Mission. *Space Science Reviews 91*, 197–242. https://doi.org/10.1023/A:1005263510820

Sandel, B. R., Goldstein, J., Gallagher, D. L., & Spasojevic, M. (2003). Extreme ultraviolet imager observations of the structure and dynamics of the plasmasphere. *Space Science Reviews*, *109*, 25-46. https://doi.org/10.1023/B:SPAC.0000007511.47727.5b

Sandhu, J. K., Yeoman, T. K., Fear, R. C., & Dandouras, I. (2016). A statistical study of magnetospheric ion composition along the geomagnetic field using the Cluster spacecraft for *L* values between 5.9 and 9.5. *Journal of Geophysical Research: Space Physics*, *121*, 2194–2208. https://doi.org/10.1002/2015JA022261

Sheeley, B. W., Moldwin, M. B., Rassoul, H. K., & Anderson, R. R. (2001). An empirical plasmasphere and trough density model: CRRES observations. *Journal of Geophysical Research*, *106*(A11), 25,631–25,641. https://doi.org/10.1029/2000JA000286

Spasojević, M., Goldstein, J., Carpenter, D. L., Inan, U. S., Sandel, B. R., Moldwin, M. B., & Reinisch, B. W. (2003). Global response of the plasmasphere to a geomagnetic disturbance. *Journal of Geophysical Research*, *108*, 1340. https://doi.org/10.1029/2003JA009987, A9

Takahashi, K., Denton, R. E., Anderson, R. R., & Hughes, W. J. (2006). Mass density inferred from toroidal wave frequencies and its comparison to electron density. *Journal of Geophysical Research*, *111*, A01201. https://doi.org/10.1029/2005JA011286

Takahashi, K., Denton, R. E., Kurth, W., Kletzing, C., Wygant, J., Bonnell, J., et al. (2015). Externally driven plasmaspheric ULF waves observed by the Van Allen Probes. *Journal of Geophysical Research: Space Physics*, *120*, 526–552. https://doi.org/10.1002/2014JA020373

Takahashi, K., Ohtani, S., Denton, R. E., Hughes, W. J., & Anderson, R. R. (2008). Ion composition in the plasma trough and plasma plume derived from a Combined Release and Radiation Effects Satellite magnetoseismic study, *Journal of Geophysical Research*, *113*, A12203. https://doi.org/10.1029/2008JA013248

Tsyganenko, N. A. (2002). A model of the near magnetosphere with a dawn-dusk asymmetry 1. Mathematical structure. *Journal of Geophysical Research*, *107*(A8). https://doi.org/10.1029/2001ja000219

Vellante, M., & Förster, M. (2006). Inference of the magnetospheric plasma mass density from field line resonances: A test using a plasmasphere model. *Journal of Geophysical Research*, *111*, A11204. https://doi.org/10.1029/2005JA011588

Vellante, M., Förster, M., Villante, U., Zhang, T. L., & Magnes, W. (2007). Solar activity dependence of geomagnetic field line resonance frequencies at low latitudes. *Journal of Geophysical Research*, *112*, A02205. https://doi.org/10.1029/2006JA011909

Vellante, M., Lühr, H., Zhang, T. L., Wesztergom, V., Villante, U., De Lauretis, M., et al. (2004). Ground/satellite signatures of field line resonance: A test of theoretical predictions, *Journal of Geophysical Research*, *109*, A06210. https://doi.org/10.1029/2004JA010392

Villante, U., Vellante, M., Francia, P., De Lauretis, M., Meloni, A., Palangio, P., et al. (2006). ULF fluctuations of the geomagnetic field and ionospheric sounding measurements at low latitudes during the first CAWSES campaign. *Annales Geophysicae*, *24*, 1455−1468. https://doi.org/10.5194/angeo-24-1455-2006

Waters, C. L., Menk, F. W., & Fraser, B. J. (1994). Low latitude geomagnetic field line resonance: Experiment and modeling, *Journal of Geophysical Research*, *99*(A9), 17,547−17,558, https://doi.org/10.1029/94JA00252

Wygant, J. R., Bonnell, J. W., Goetz, K., Ergun, R. E., Mozer, F. S., Bale, S. D., et al. (2013). The electric field and waves instruments on the Radiation Belt Storm Probes mission. *Space Science Reviews*, *179*, 183–220. https://doi.org/10.1007/s11214-013-0013-7

Zhelavskaya, I. S., Spasojevic, M., Shprits, Y. Y., & Kurth, W. S. (2016). Automated determination of electron density from electric field measurements on the Van Allen Probes spacecraft. *Journal of Geophysical Research: Space Physics*, *121*, 4611–4625. https://doi.org/10.1002/2015JA022132

Table 1. CARISMA station pairs employed[a]

Station pair	Geog. Lat. (°N)	Geog. Lon. (°E)	CGM Lat. (°N)	CGM Lon. (°E)	*L*	MLT	CGM Lat.Separ. (°)	CGM Lon.Separ. (°)
FCHP-MCMU	57.72	248.84	64.95	310.69	5.68	UT – 7.91 h	2.06	0.54
MCMU-MSTK	55.00	247.91	62.16	310.28	4.67	UT – 7.94 h	3.52	1.35
MSTK-VULC	51.86	247.03	58.93	309.99	3.83	UT – 7.96 h	2.94	0.74
VULC-POLS	49.02	246.41	56.02	309.90	3.26	UT – 7.97 h	2.90	0.88

[a]*L* shell, geomagnetic coordinates, and MLT are calculated for 2015 at 120 km altitude

Table 2. Ground-space conjunction intervals

N	Probe	Orbit n.	Date	DoY	start-end time (hh.mm.ss)
1	RBSP-A	2744	22 June, 2015	173	12.55.00-14.20.00
2	RBSP-A	2752	25 June, 2015	176	12.20.00-13.25.00
3	RBSP-A	2760	28 June, 2015	179	12.05.00-14.10.00
1	RBSP-B	2729	22 June, 2015	173	13.30.00-15.25.00
2	RBSP-B	2737	25 June, 2015	176	13.30.00-17.00.00
3	RBSP-B	2745	28 June, 2015	179	13.55.00-17.40.00

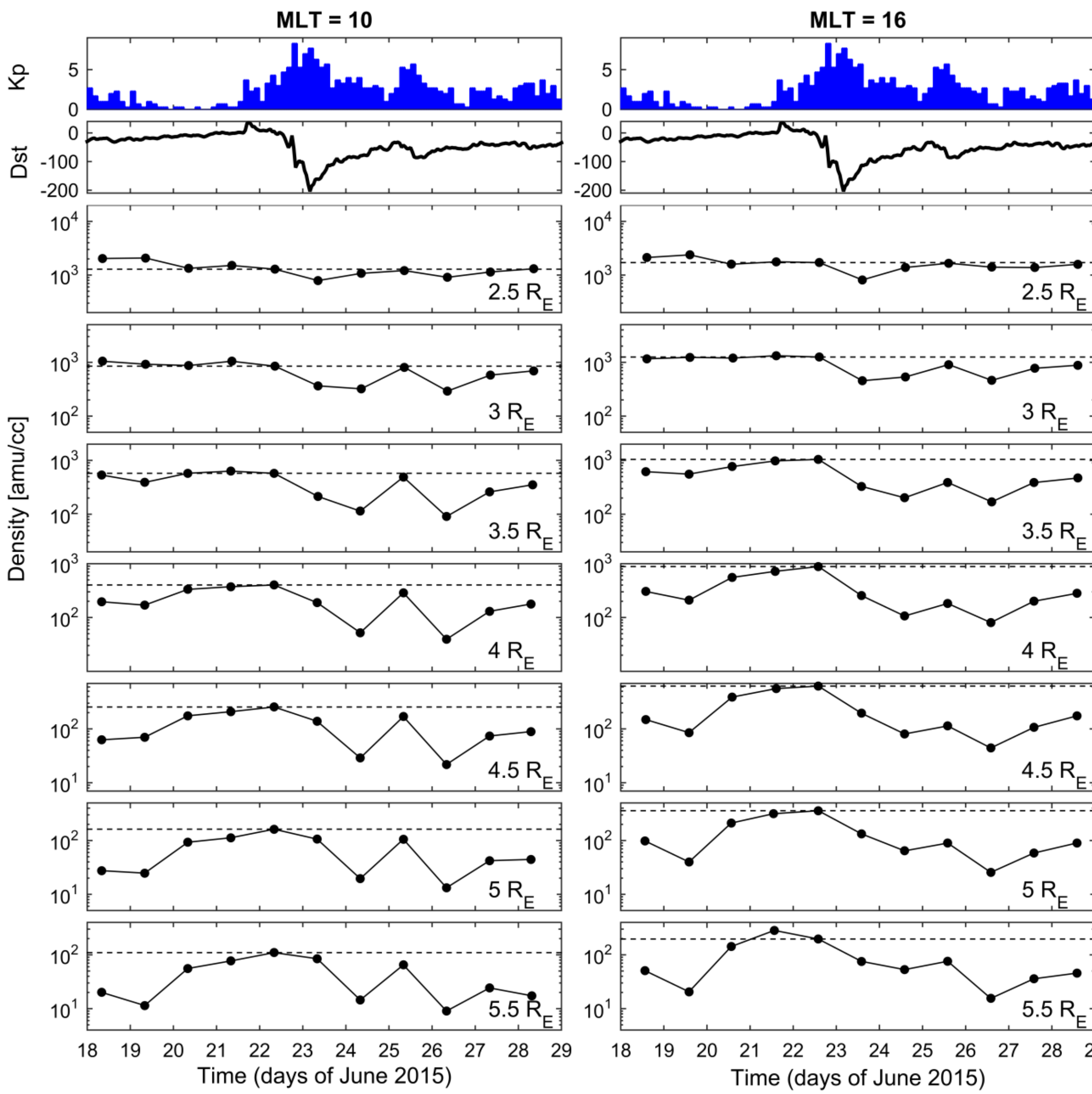

684 **Figure 1.** Day-to-day variation of the equatorial plasma mass density at different geocentric distances and for two different Magnetic Local Times, derived from field line resonance frequencies detected at the EMMA magnetometer network. Top panels show the Kp and Dst indices.

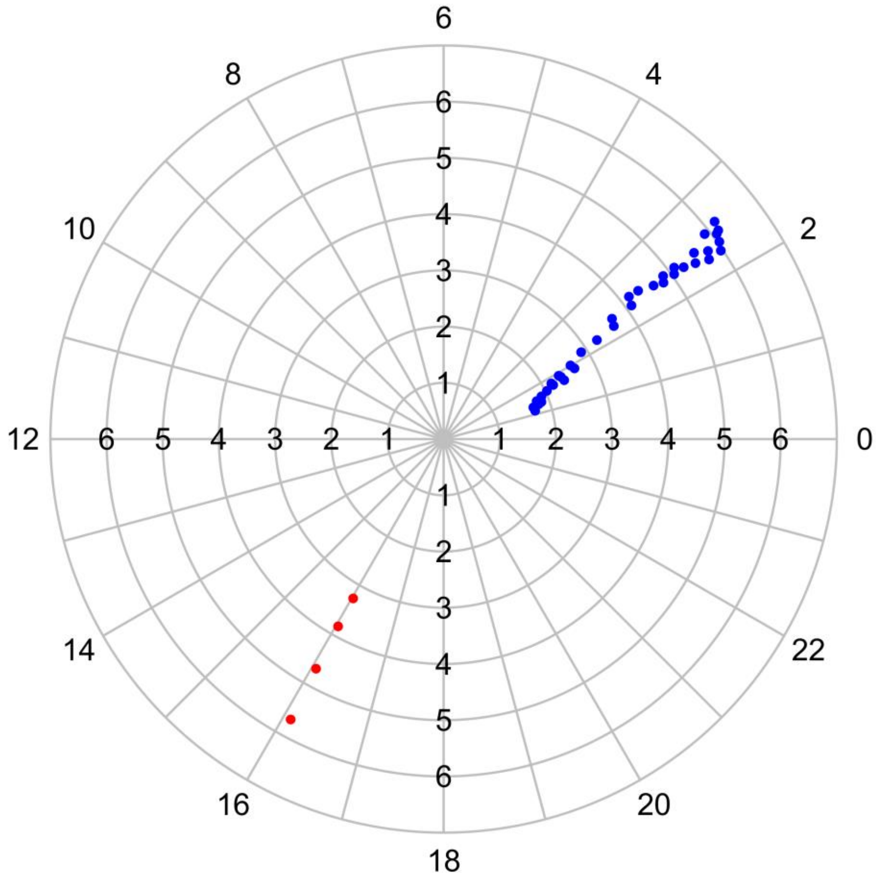

Figure 2. Locations of station pair midpoints for EMMA (blue dots) and CARISMA (red dots) in *L*-MLT coordinates. Values reported around the outermost circle are the difference between MLT and UT.

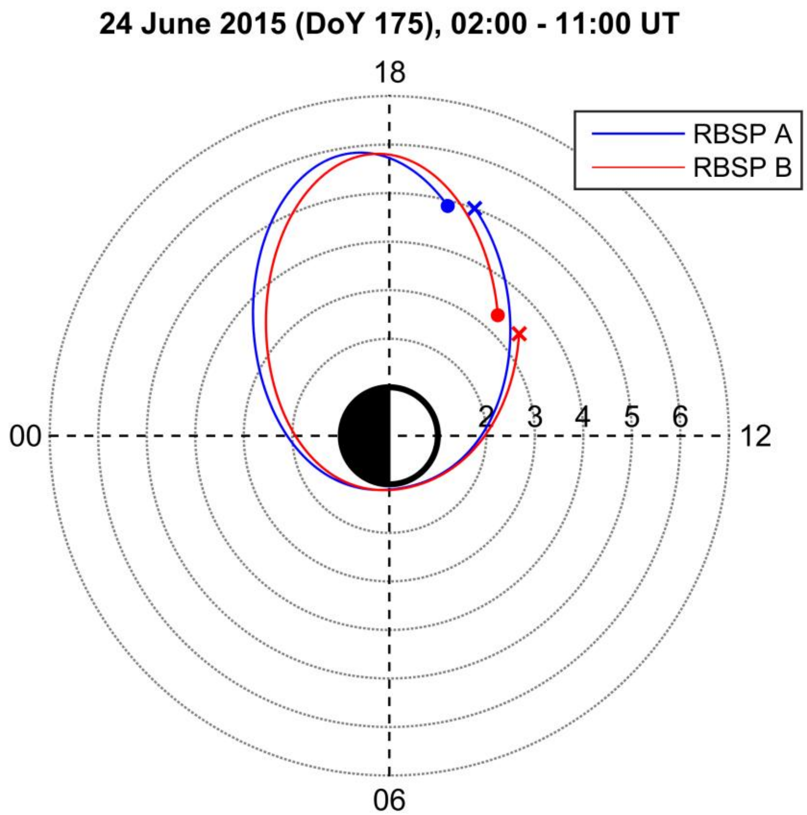

Figure 3. RBSP orbits in *L*-MLT coordinates (calculated using a centered dipole) during 0200-1100 UT on 24 June 2015. Locations at start/end times are indicated by dots/crosses.

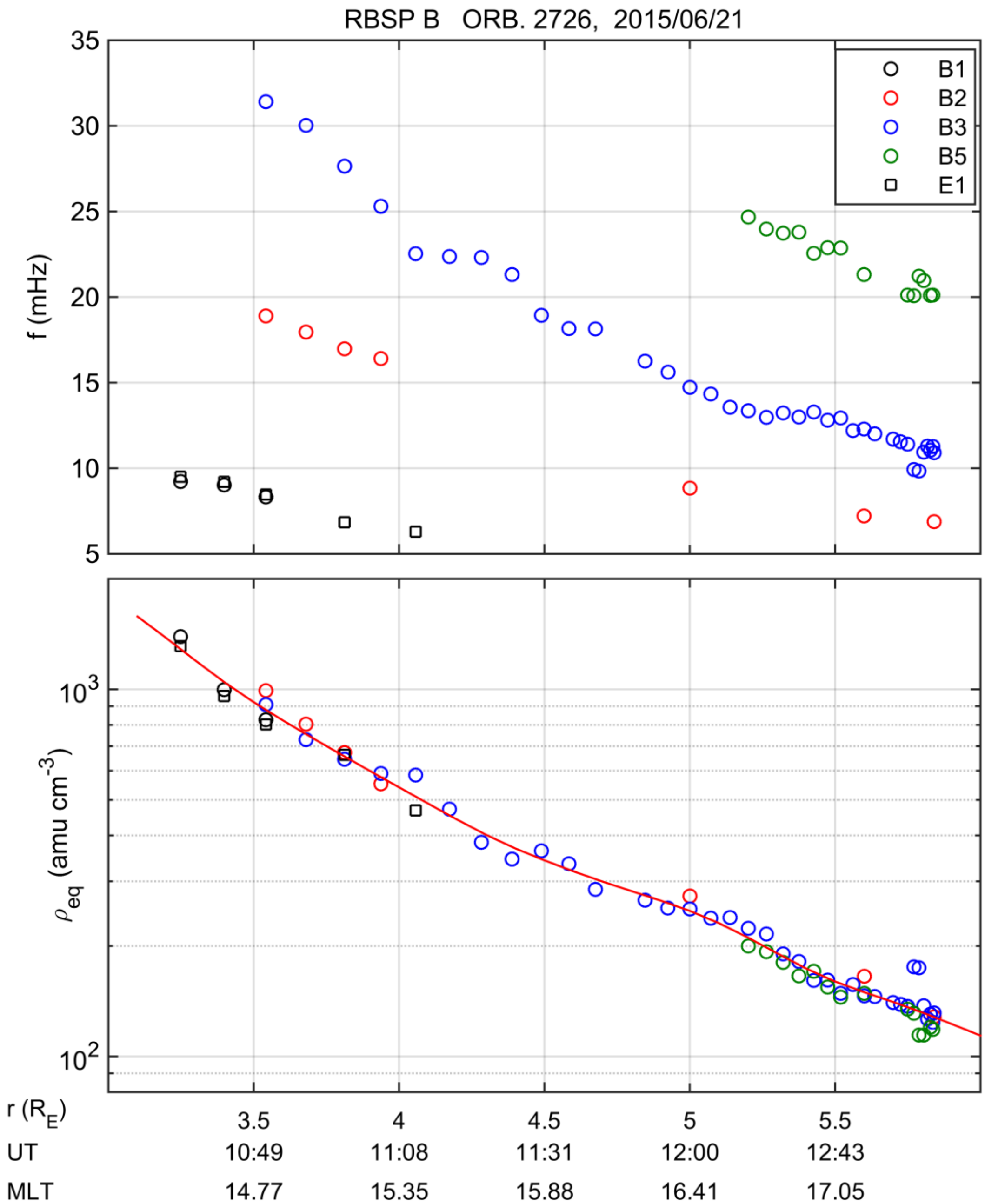

695 **Figure 4.** Top panel: Selected harmonic frequencies for the outbound leg of the orbit n. 2726 of
696 RBSP B on 21 June 2015. Bottom panel: Corresponding estimates of the equatorial plasma mass
697 density. See text for details.
698

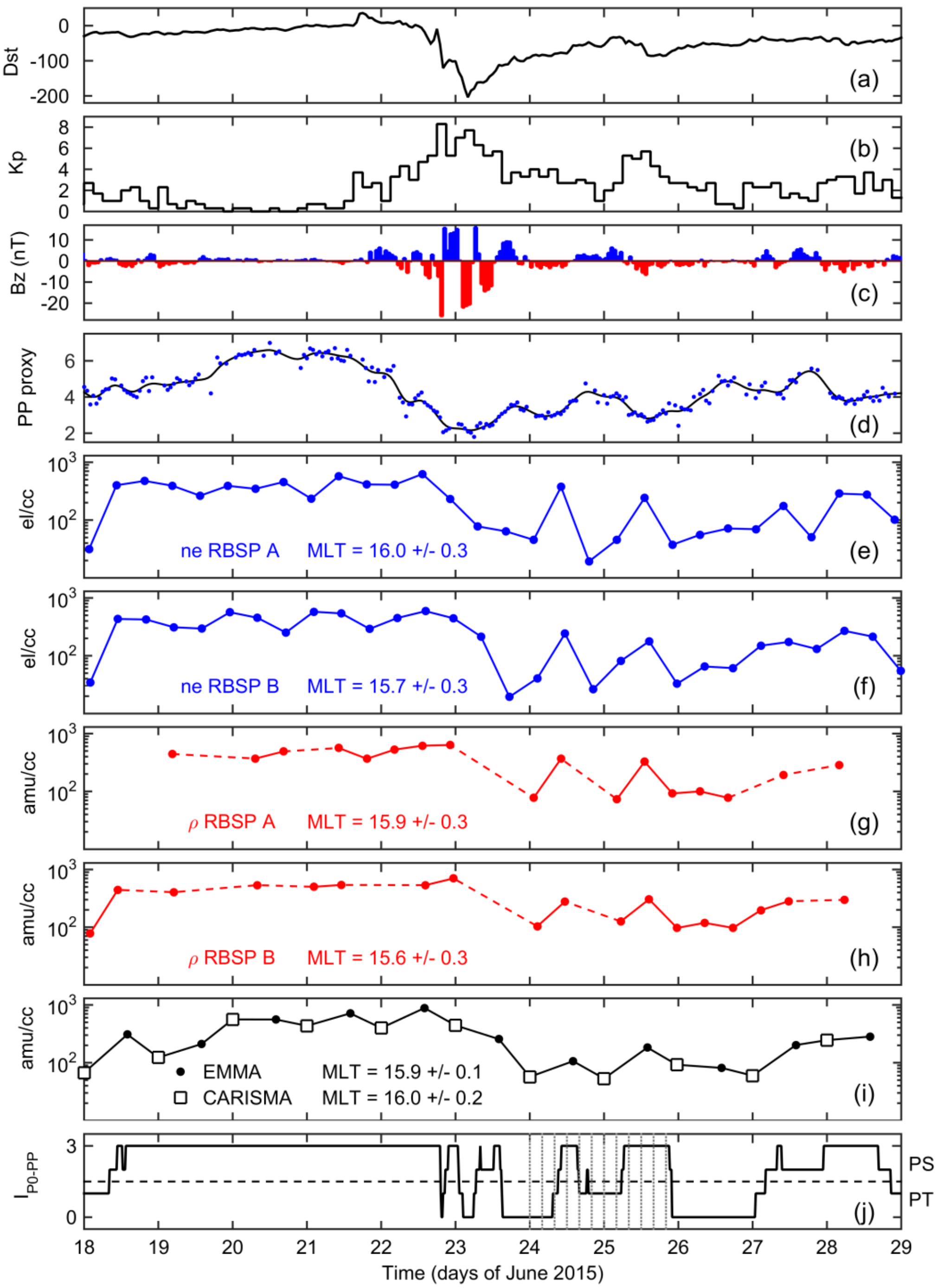

Figure 5. (a-d) Kp, Dst, $B_{Z,IMF}$ in GSM coordinates (red/blue colours indicate southward/nortward direction), and midnight plasmapause proxy during 18-28 June 2015. (e-i) Plasma density evaluated at L = 4, 16 MLT: (e, f) RBSP-NURD electron density; (g, h) plasma mass density from RBSP-FLR measurements; (i) plasma mass density from EMMA/CARISMA-FLR observations. (j) Virtual observations from the plasmapause test particle simulation in terms of the I_{P0-PP} index defined in section 2.3. Values above/below the horizontal dashed line mean that the monitored point is in plasmasphere (PS)/plasmatrough (PT).

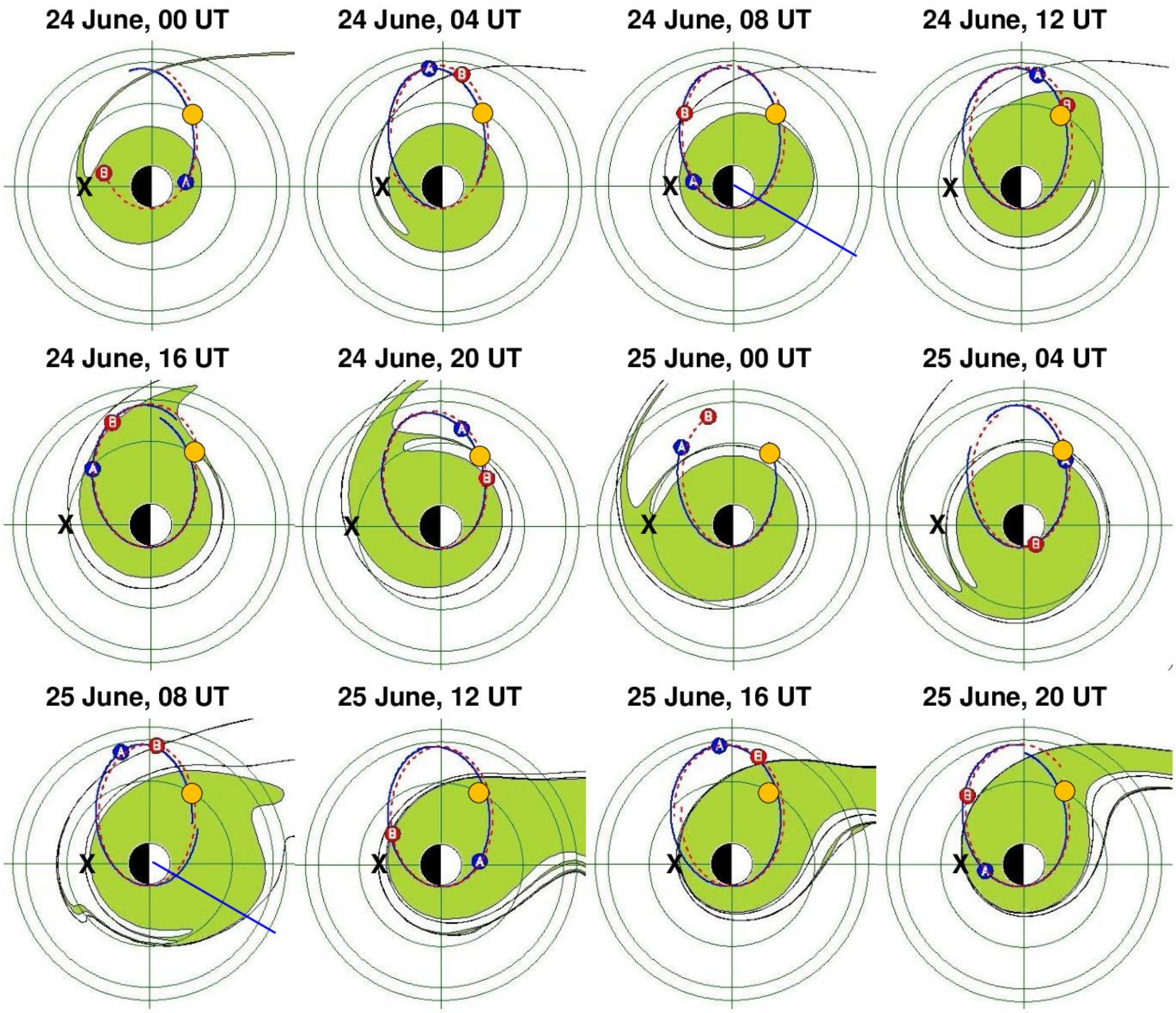

Figure 6. Output of the plasmapause test particle simulation with a time step of 4 hours during 24-25 June 2015. The green regions represent the simulated plasmasphere. Circles are drawn at 4, 6, and 6.6 R_E. Also shown are the orbits and locations of RBSP A (red) and RBSP B (blue), the monitored point at L = 4, 16 MLT (orange dot), and the midnight plasmapause location as determined from Swarm observations (black cross). The blue straight lines drawn at 08 UT of both days indicate 10 MLT.

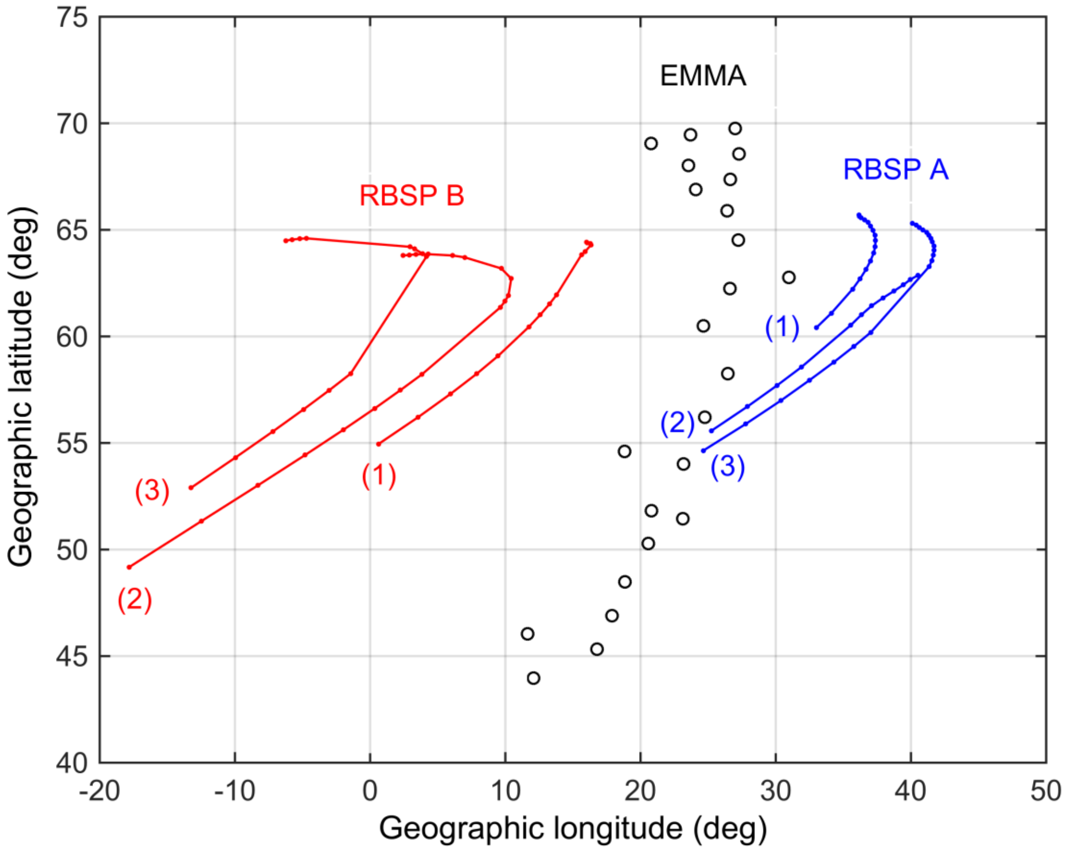

Figure 7. Geographic locations of the EMMA stations and the RBSP magnetic field footprints for six different conjunction intervals (see Table 2). Footprints are determined using the T02 magnetic field model.

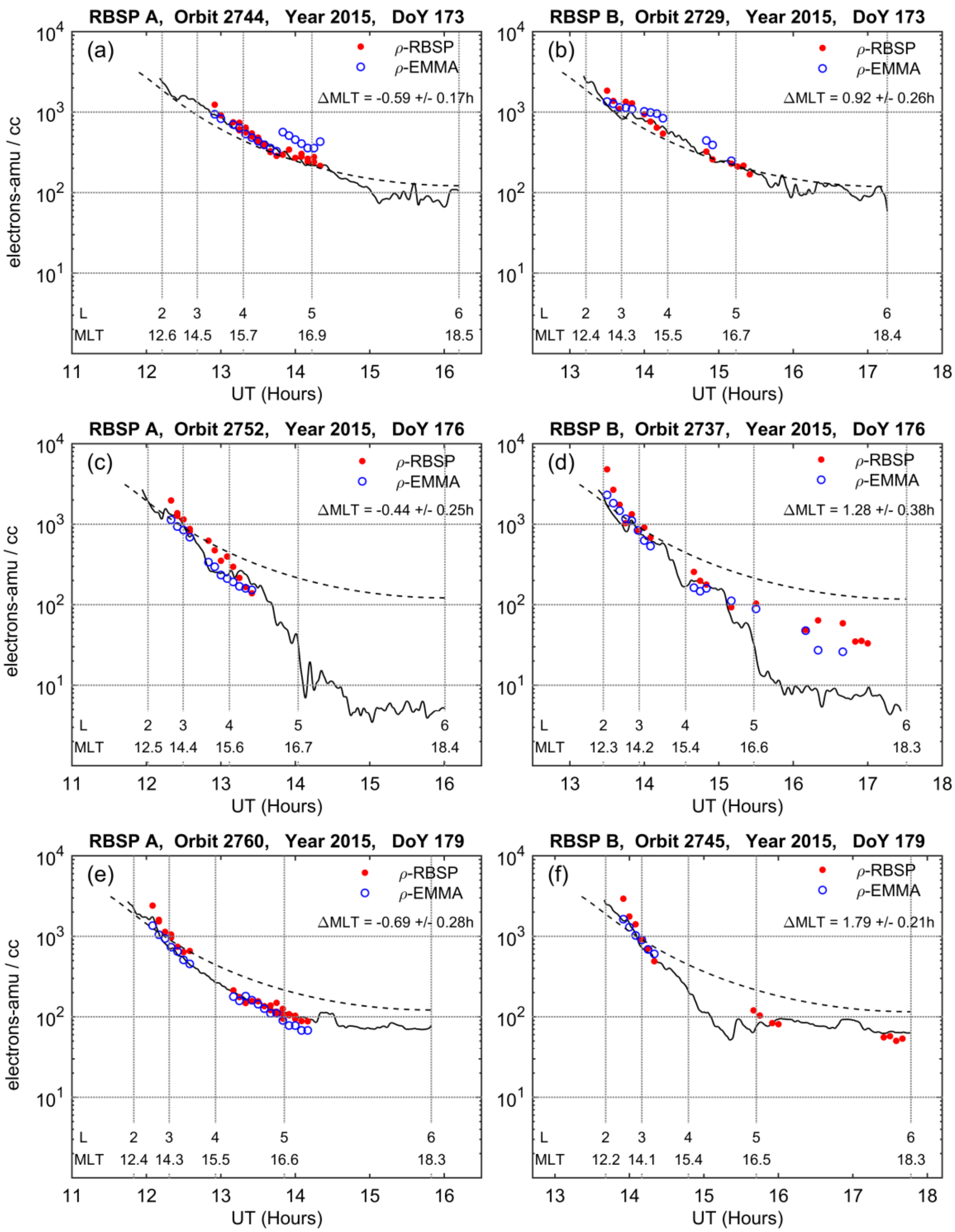

Figure 8. Comparison between RBSP-equatorial mass densities (red points), EMMA-equatorial mass densities (blue open circles), and NURD-equatorial electron densities (black solid line) for the six conjunction intervals listed in Table 2. Dashed curve is the Carpenter and Anderson (1992) saturated plasmasphere electron density model. Dotted vertical lines are drawn at L = 2, 3, 4, 5, 6. The mean MLT deviation between EMMA and RBSP measurements is indicated inside each panel. See text for more details.

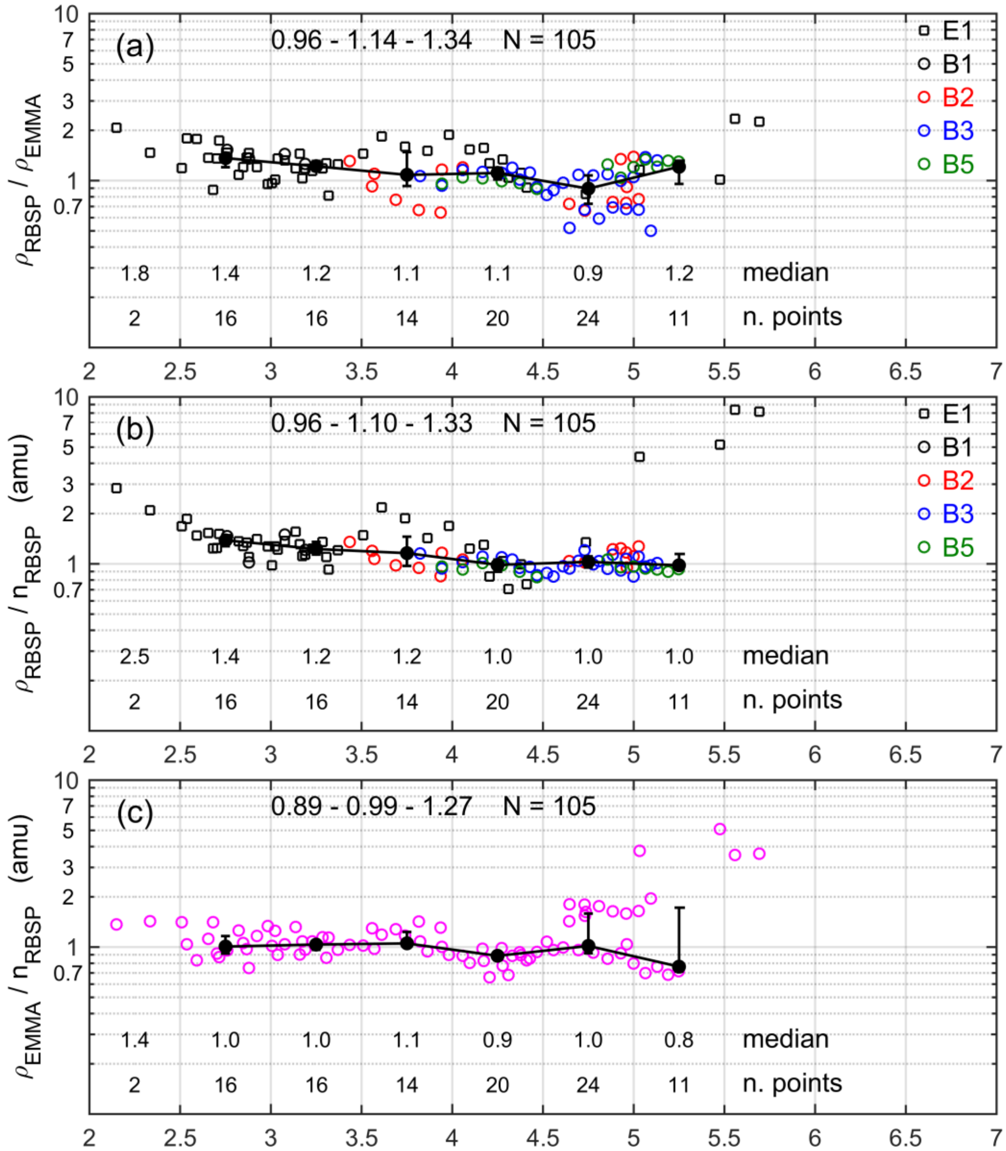

Figure 9. (a) Ratio between RBSP/FLR-derived and EMMA/FLR-derived plasma mass density for the conjunction intervals as a function of the equatorial distance. The different markers/colors indicate from which harmonic the RBSP estimate was obtained. Black dots connected by straight lines are the medians in r_{eq} bins, and the vertical bars connect the lower and upper quartiles. Lower quartile, median, and upper quartile of the whole population are indicated on the top. Number of samples and medians for each bin are indicated above the horizontal axis. (b) The same as (a) but for the ratio between RBSP/FLR-derived plasma mass density and RBSP/NURD electron number density (average ion mass). (c) The same as (b) but for the ratio between EMMA/FLR-derived plasma mass density and NURD electron number density.

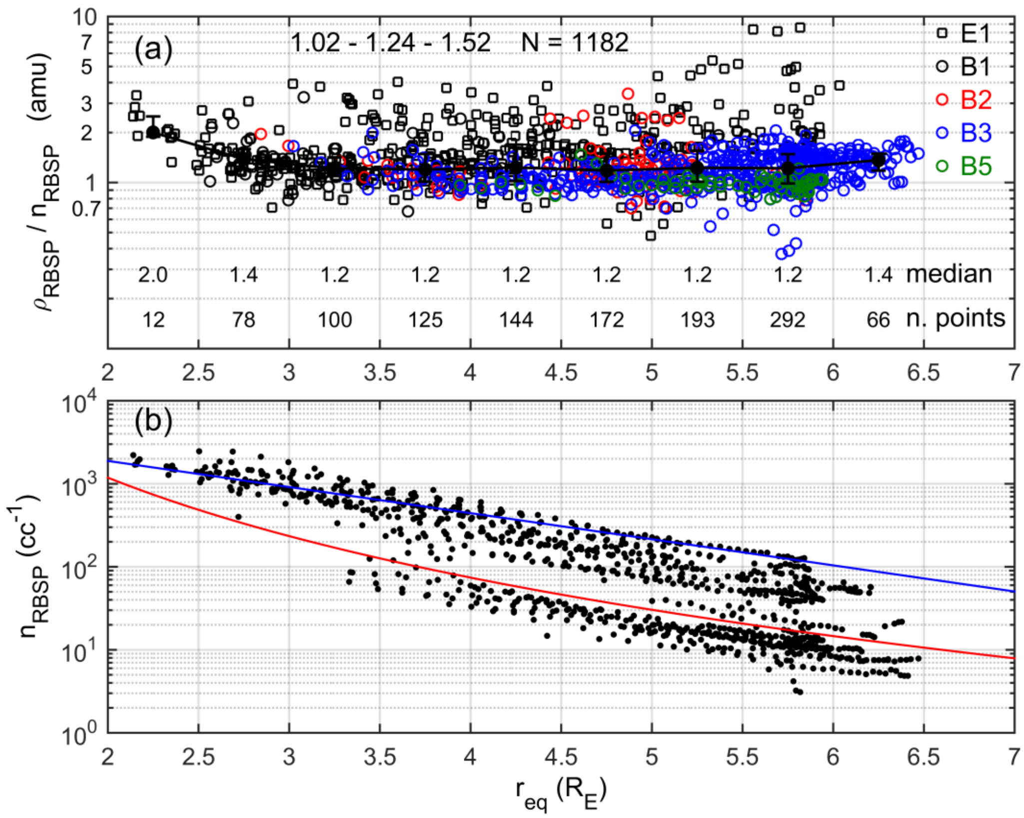

Figure 10. (a) The same as in Figure 9b but for the whole RBSP/FLR data set. (b) Electron number density (black dots) as a function of the equatorial distance. The red line is the empirical criterion for separating plasmaspheric-like from trough-like observations (Sheeley et al., 2001). The blue line is the Carpenter and Anderson (1992) saturated plasmasphere electron density model.